Hot-spot detection and characterization of strombolian activity from MODIS infrared data

Published version:

DOI:10.1080/01431161.2014.903354

(Article begins on next page)

Hot-spot detection and characterization of strombolian activity from MODIS infrared data

by

Coppola, D., Laiolo, Delle Donne, D., Ripepe, M., Cigolini C. (2014). International Journal of Remote Sensing, 35/9, 3403-3426.

http://dx.doi.org/10.1080/01431161.2014.903354

Detection and characterization of variable thermal regimes at Stromboli volcano from MODIS infrared data

D. Coppola[1a], M. Laiolo[a], D. Delle Donne[b], M. Ripepe[b], C. Cigolini[a,c]

[a]Dipartimento di Scienze della Terra, Università di Torino, Via Valperga Caluso 35, 10125 Torino, Italy;
[b]Dipartimento di Scienze della Terra, Università di Firenze, Via G. La Pira,4 - 50121 Firenze, Italy;
[c]NatRisk, Centro Interdipartimentale sui Rischi Naturali in Ambiente Montano e Collinare, Università degli Studi di Torino, Italy.

Identifying and characterizing strombolian activity from space is a challenging task for satellite-based infrared systems. Stromboli volcano is a natural laboratory that offers a unique opportunity for refining thermal remote sensing applications that involve transient phenomena and small to moderate hot-spots. A new simple and fast algorithm gave us the opportunity to revisit the MODIS-derived thermal output at Stromboli volcano in the last 13 years. The new algorithm includes both nigthttime and daytime data and shows a high performance with the detection of small-amplitude thermal anomalies (< 1 MW), as well as a low occurrence of false alerts (< 4%). Here, we show that the statistical distribution of Volcanic Radiative Power (*VRP*; in Watt) is consistent with the detection of variable activity regimes that we subdivided into six levels of thermal activity: Very Low (*VRP* < 1 MW), Low (1 MW < *VRP* < 15 MW), Moderate (15 MW < *VRP* < 80 MW), High (80 MW < *VRP* < 315 MW), Very High (315 MW < *VRP* < 1000 MW), Extreme (*VRP* > 1000 MW). The "Low" and "Moderate" thermal levels are associated to strombolian activity and reflect fluctuations of the magma level within the conduit feeding the activity at the surface. The "High" and "Very High" levels of thermal output represent the bulk thermal emissions during periods of effusive activity. The most highly level ("Extreme") is reached only during the onset of flank eruptions (occurred on 28 December 2002 and 27 February

[1] * Corresponding Author. Email: diego.coppola@unito.it

2007). We found that the retrieved thermal levels are in general agreement with the explosive levels evaluated at Stromboli since 2005, and their correlation has been shown to be dependant on the observed activity (i.e. eruption onset, lateral flank effusion, summit overflows, strombolian activity). The specific hot spot detection system presented here allow us to characterise thermal emissions in terms of different levels of volcanic activity, to decode the thresholds separating them and to depict long term eruptive dynamics at open-vent volcanoes.

1. Introduction

In the last decade thermal remote sensing techniques have been increasingly applied for monitoring active volcanoes. Ramsey and Harris (2013) give an overview of these applications, discussing the limits of several satellite-based infrared sensors to detect and track volcanic hot-spot. Actually, many of these studies are concentrated in developing near real time automated techniques thus quantifying the heat released and the related mass fluxes (Ganci et al., 2012).

A variety of algorithms were developed for detecting volcanic hot spots using different satellites and sensors, such as GOES (e.g. Harris et al., 1997), AVHRR (e.g. Harris et al. 1995; Tramutoli 1998), MODIS (e.g. Flynn et al. 2002; Wright et al. 2002), SEVIRI (Hirn, Di Bartola, and Ferrucci 2009; Ganci et al., 2011). A comprehensive review of these techniques, including their performance and applicability, is given by Steffke and Harris (2011). According to the authors, these algorithms may be subdivided into four main groups on the basis of their detection principles. These are:

(i) *fixed threshold*: which use the data on a single pixel to assess whether the radiance or temperature, is anomalous (i.e. Flynn et al., 2002, Wright et al. 2002);

(ii) *contextual*: it uses the difference between a pixel's radiance (or temperature) and the surrounding pixels to assess the presence of an hot spot (i.e. Harris et al, 1995; 2001; Harris, Pilger, and Flynn 2002; Higgins and Harris 1997; Kaneko et al., 2002; Webley et al., 2008; Galindo and Dominguez, 2003);

(iii) *temporal*: it compares a pixel's radiance (or temperature) with mean values obtained for the same pixel from time series of data (i.e. Di Bello et al., 2004; Pergola, Marchese, and Tramutoli 2004);

(iv) *hybrid*: it combines two or more of the above principles (i.e. Dean et al., 1998; Dehn, Dean, and Engle 2000; Kervyn et al., 2006; Hirn, Di Bartola, and Ferrucci 2009; Koeppen, Pilger, and Wright, Glaze, and Baloga 2011).

In their review Steffke and Harris (2011) concluded that each algorithm operates well within the limits and criteria of its design requirement. For example, a global detection system such as MODVOLC (Flynn et al., 2002, Wright et al. 2002) has a lower efficiency in detecting hotspots, but favours the processing of a large amount of data in near real time. On the other hand, the algorithm based on the simple temporal principles (i.e. the RST technique of Di Bello et al., 2004) may be more efficient in detecting local small hotspots, but requires more complex data processing and is somehow inefficient to provide a continuous record of persistent, stationary thermal anomalies (Koeppen, Pilger, and Wright 2011, Steffke and Harris, 2011). The efficiency of any hot-spot detection system may effectively change in function of the observed volcanic activity. Effusive eruptions are easier case to be detected since they represent volcanic targets with high surface temperatures and widespread thermal anomalies (lava flows). Conversely, hot-spots detection over active lava domes is more challenging since these bodies have smaller planar dimensions and cooler lava surfaces (Wright, Glaze, and Baloga 2011). Moreover, the persistence of a thermal anomaly is a further complication for space-based hot-spot detection. For instance, short-lived phenomena (such as explosions or short paroxysms) produce transient thermal signals with small probabilities of being detected. If these events are associated to a small size hot emitters (i.e., a volcanic vent and/or vents), they represent critical targets. For these reasons the detection of "strombolian activity" from space represent one of the challenging task for satellite-based infrared systems (e.g., Coppola et al., 2012).

Stromboli is an open-system volcano, located in the Aeolian islands (Southern Tyrrhenian Sea; Figure 1) well known for its permanent volcanic activity considered as a reference case for classifying minor to intermediate volcanic eruptions (e.g., Newhall and Self, 1982). Volcanic activity is essentially strombolian, with continuous explosions and mild eruptions of scoriae, lapilli, ash and bombs (Rosi, Bertagnini, and Landi 2000) at summit vents. This activity may be sporadically replaced by lava effusions and more energetic explosions with the eruption of larger volumes of tephra, named "paroxysms" (Barberi, Rosi, and Sodi 1993).

At Stromboli, the climate is temperate with higher temperatures reaching 36-40 °C during the summer (July) and minima temperatures of 0-4 °C during the winter time (December and January). The rainfall is not abundant and widely distributed in about 50-90 days a year of rain with a peak in the cold season. The month with the lowest number of rainy days is July, whereas December and January have the highest number of rainy days (cf., Laiolo et al., 2012). The sky is clear for 35% of the days in spring, 70% in summer, 50% in the fall and 25 % in the winter. Snow has been rarely observed at the summit of the volcano (924 m asl). Due to the peculiar volcanic activity and its temperate climate Stromboli volcano may be considered as a natural laboratory for refining infrared remote sensing applications.

Figure 1

In this paper we describe a new algorithm, specifically developed for hot-spot detection at Stromboli volcano. Thus, the new algorithm is addressed to detect small thermal anomalies and contains spectral (threshold), spatial (contextual) and temporal principles well compatible with the so-called "*hybrid*" approach (e.g., Koeppen, Pilger, and Wright 2011). Here, we analyze more than a decade of MODIS data collected on Stromboli by revisiting and updating the earlier analyses of Coppola et al. (2012). After showing the algorithm performance, we will show how the long term thermal records may be used to define distinct thermal regimes that characterize the recent activity of Stromboli.

2. The algorithm

The algorithm uses MODIS level 1b data acquired by NASA's Terra (launched on December 1999) and Aqua (launched on May 2002) satellites that normally image Stromboli volcano four times per day (since May 2002). The whole data set (from March 2000 to March 2013), consisting of more than 19000 images, has been analysed following several main steps. These are: (*i*) Data Extraction, (*ii*) Resampling, (*iii*) Definition of Region of Interest (ROIs), (*iv*) hot-spot detection (*v*) calculation of the Volcanic Radiative Power (VRP).

2.1. Data Extraction from MODIS level1b granules

The first step is dealing with the extraction of the data from the MODIS level1 granules. These data consist of the date and time of satellite overpasses, the satellite viewing geometry (zenith and azimuth), the location of each pixel (Latitude and Longitude) as well as the Digital Number (DN) related to the spectral bands of interest:

(i) Reflectivity of band 1 (R_1), centred at 0.645 μm (for daytime image only)

(ii) Reflectivity of band 2 (R_2), centred at 0.858 μm (for daytime image only)

(iii) Radiance of band 6 (L_6), centred at 1.64 μm (for daytime image only)

(iv) Radiance of band 21 (L_{21}), centred at 3.959 μm (Low-gain MIR channel)

(v) Radiance of band 22 (L_{22}), centred at 3.959 μm (High-gain MIR channel)

(vi) Radiance of band 31 (L_{31}), centred at 11.03 μm (TIR channel)

(vii) Radiance of band 32 (L_{32}), centred at 12.02 μm (TIR channel)

The DN of each selected band is firstly scanned to filter-out any missed or "corrupted" datum. According to the MODIS Level 1B Product User's Guide (Toller, Isaacman, and Kuyper 2006) this is achieved by eliminating, for each band, all the pixels with DN > 32,768 (i.e., the invalid data values), with the exception of the pixels with DN = 65,533 (saturated values), used in the subsequent steps.

The georeferred data are also scanned to remove the bow-tie effect that, at the edge of the swath, produces the so called "scan to scan" overlapping (Nishihama et al. 1997).

Once the effects of invalid and bow-tie related pixels have been removed, we used the conversion coefficients for each selected band (scale and offset) in order to convert the DN into reflectivity and/or radiance data (for details regarding this step see the MODIS Level 1B Product User's Guide).

Finally, we build up a corrected spectral band centred at 3.959 μm (hereby called band L_{21ok}), by using the L_{21} or L_{22} radiance, depending on band 22 saturation (or not), respectively.

2.2. Resampling of original data and production of NTI maps

Cropping and resampling of the original Level1b MODIS data is necessary for two main reasons. First because high scan angles contribute to the growth of the projected ground spatial element (up to approximately 10 km^2 for scan angles of 55°; Nishihama et al. 1997). This leads the radiance of a potential sub-pixel hotspot to be integrated over a variable area, thus introducing a further source of error in estimating its thermal output. Secondly, because the hot-spot detection scheme, described below, requires an image-to-image registration, similar to application of the RST technique (cf. Di Bello et al. 2004; Pergola, Marchese, and Tramutoli 2004).

Thus, we cropped and resampled (into an equally-spaced 1 km grid) the MODIS level1b data which fall within a mask (50 x 50 km) centred over the summit of Stromboli volcano (Figure 2(*a*)). This means that one hot-spot pixel, whose area was 2 km^2 in the original image, become two pixels with equal areas of 1 km^2 in the resampled image.

Once the radiances data has been resampled we calculated the Normalised Thermal Index (NTI) for each pixel according to Wrigth et al. (2002):

$$NTI = \frac{L_{21ok} - L_{32}}{L_{21ok} + L_{32}} \quad (1)$$

These *NTI* maps enhance the presence of any sub-pixel hotspot and represents the reference matrices to the further steps of the algorithm.

Figure 2

2.3. Regions of Interest

A main step in the processing flowchart is the definition of three Regions Of Interest (ROIs) within the resampled NTI maps. These are centred on the volcano summit (where strombolian activity is taking place) and are normally concentric (see Figure 2*(b)*). The ROI_1 consists of an outer ring (measuring 50 x 50 km) and includes the island of Panarea as well as the sea surrounding Stromboli. The ROI_2 represents an intermediate region (15 x 15 km) essentially characterized by the sea surrounding the island of Stromboli. Finally, the ROI_3 (5 x 5 km) samples the island of Stromboli itself, including the coast lines and small portions of its near-shore sea.

2.4. Hot Spot detection

The algorithm is based on the characterization of the natural variation of the *NTI* (seasonal effect) within each ROI. For example in Figure 2 we plot the *NTI* time-series relative to the nighttime pixels of each ROI during 2006. Note that within this plot, the thermal anomalous pixels (hot-spot contaminated) tend to increase their *NTI*, whereas the presence of thick and cold clouds has the opposite effect and tend to lowering their relative values (negative spikes).

Figure 3

The seasonal variation of the NTI is clear in the three regions although some anomalous pixel is consistent with the presence of some hot-spot within ROI_3 (Figure 3*(a)*).

In the next sections we describe the algorithm subdivided for nighttime and daytime data, respectively.

2.4.1. Nighttime algorithm

To detect an hot-spot within the nighttime images we firstly defined two fluctuating thresholds (named $NTI_{thresh1}$ and $NTI_{thresh2}$, respectively) that envelop the natural variation of the NTI within the whole image (including ROI_1, ROI_2 and ROI_3; Figure 2*(b)*) in absence of thermal anomalies and/or cloud covering. These thresholds are obtained by using the form of a typical sinusoidal function which can be described by:

$$NTI_{thresh} = A\sin\left[\frac{2\pi}{P}(t-\alpha)\right]+C \qquad (2)$$

where A is the yearly amplitude of the NTI variation, P is the length of each cycle (Π/days), t is the time of satellite overpass (julian day), α is the phase shift (i.e., the day when the curve crosses the baseline as it ascend), and C is the baseline, here represented by the average yearly NTI value.

To set the appropriate parameters for the two thresholds (Equation 2), it is necessary to process at least one year of data. Hence, the operator may chose the appropriate values of A, α and C by excluding the pixels clearly contaminated by hot-spot and clouds (with NTI values that clearly deviate from the seasonal trend). The values assumed for Stromboli volcano are summarised in Table 1 with their relative NTI thresholds plotted in Figure 3.

These two thresholds define three fields on the *NTI* timeseries, where the upper and lower fields represent the sectors where hot-spot contaminated and cloud contaminated pixels are surely present (Figure 3).

At this point a pixel is considered “alerted” (hot-spot contaminated) if at least one of the following test is successfully passed.

The first test is applied to all the pixels of an image (NTI_{ROIS}) and requires that the *NTI* is higher than $NTI_{thresh1}$:

$$Alert1 = NTI_{ROIS} > NTI_{thresh1} \qquad \text{[Test 1]}$$

The second test is applied for detecting exclusively the smallest thermal anomalies of ROI_3 having an *NTI* comprised between $NTI_{thresh1}$ and $NTI_{thresh2}$. This is achieved by comparing the *NTI* of each ROI_3-pixel (not previously alerted by the Test 1) with some statistical parameters retrieved from a selected suite of “reference-pixels” appertaining to ROI_2. In particular, these “reference-pixels” (NTI_{Ref2}) are the ROI2 pixels which satisfy the following condition:

$$NTI_{Ref2} = NTI_{thresh1} > NTI_{ROI2} > NTI_{thresh2} \qquad \text{[Condition 2]}$$

Hence according to condition 2, we defined “reference-pixels” all the pixels of ROI_2 which have the *NTI* comprised between the two thresholds previously defined ($NTI_{thresh1}$ and $NTI_{thresh2}$). In other words, NTI_{Ref2} exclusively includes the pixels surrounding Stromboli volcano that are not contaminated by hot-spots or clouds.

From these reference pixels we thus calculate the maximum value (NTI_{Max2}), mean (NTI_{Mean2}) and the standard deviation (NTI_{std2}) which are the parameters used to define the second test:

$$Alert2 = (NTI_{ROI3} > NTI_{Max2})\ \&\ [NTI_{ROI3} > (NTI_{Mean2} + 3 \times NTI_{std2})] \qquad \text{[Test 2]}$$

Therefore, Test 2 settles that a pixel of ROI_3, in order to be considered hot spot contaminated, must have an *NTI* higher than the value obtained by considering the natural variability of the surrounding region (ROI_2).

The total number of "alerted" pixels (*Alert*) is finally obtained by considering all the pixels passing the Test 1 (*Alert1*) or the Test 2 (*Alert 2*).

2.4.2. Daytime algorithm

The detection of hot-spot during daytime overpasses is much more complicated due to two main reasons. First, because the radiance in the MIR channel (L_{21ok}) is particularly affected by solar reflection effects (Wright et al., 2002). Solar reflection perturbs the *NTI* as well, especially for pixels that are sampling reflective surfaces (i.e. water, snow, sand, clouds, etc.), thus causing an increase in its value due to the reflected solar energy (Wright et al., 2002). Secondly, because during daytime the solar heating may effectively enhance the contrast between vegetated and non-vegetated areas. This will produce apparently higher *NTI* values over volcanic (non-vegetated) areas when compared with the surrounding (vegetated) areas. These intrinsic effects, may cause a problematic discrimination of genuine volcanic hot-spot since during daytime all the pixels in non-vegetated areas have *NTI* values that naturally exceed the surrounding background.

In the attempt to reduce the effects of solar reflection we apply a correction to the L_{21ok} radiance (on the resulting *NTI*) based on the co-registered radiance recorded on band 6 (L_6). Following Wright et al., 2004 for daytime data we thus corrected the radiance at 4µm (L_{21ok}) by subtracting 4.26% of the energy radiated at 1.6 µm (*L6*) (assumed to be the solar reflected component). The corrected NTI thus becomes:

$$NTI_{corr} = \frac{(L_{21ok} - (0.0426 * L_6)) - L_{32}}{(L_{21ok} - (0.0426 * L_6)) + L_{32}} \quad (3)$$

The comparison between the un-corrected and corrected *NTI*, relative to the 2006 day-time data is shown in Figure 3. In Figure 4*(a)*, the un-corrected *NTI* shows an extremely noisy signal in all the ROIs, overprinted on the typical seasonal trend. The noise introduced by solar reflection (represented by spikes) is particularly evident on ROI_1 and ROI_3, both related to the reflective sea surface. On the other hand, the application of Equation (3) (solar correction) produces a clear attenuation of these signals enhancing the filtered seasonal pattern. Notably, the seasonal trend and the absolute values of the NTI_{corr} relative to ROI_1 and ROI_2 (Figure 4*(b)*) become very similar to those recorded during nighttime overpasses (compare Figure 3*(b)* and 4*(b)*). This similarity suggest that the trend recorded by NTI_{corr} is almost exclusively affected by the seasonal variation of the sea surface temperature (thermal inertia of the sea makes the diurnal changes in temperature less pronounced than on land) and increases our confidence that solar contamination has been removed by applying Equation (3).

This is also confirmed by looking at the NTI_{corr} trend of ROI_3 that from April to October (i.e., during the hot season) is "diverging" from ROI_1 and ROI_2. Such a decoupling can be explained by the increase of the temperature gradient occurring between the summit, non-vegetated, volcanic areas (essentially affected by the solar heating) and the surroundings.

We therefore define a single daytime *NTI* threshold ($NTI_{thresh3}$) that allows us to discriminate between the solar heating effects and the presence of a genuine volcanic hot-spot. As previously, we used Equation (2) to describe the seasonal $NTI_{thresh3}$ trend (Figure 4*(b)*). The parameters for calculating $NTI_{thresh3}$ are summarized in Table 1. We thus flagged a thermal alert whenever a daytime pixel satisfies the following test:

$$\text{Alert3} = \text{NTI}_{\text{ROIS}} > \text{NTI}_{\text{thresh3}} \qquad \text{[Test 3]}$$

As it will be discussed later, the capability of detecting hot-spot during daytime is much more reduced when compared to the application of the nighttime algorithm. This results in poor detection rates during periods of low strombolian activity. However, during periods of more vigorous thermal activity, as well as during the effusive eruptions, the results of the daytime algorithm will strongly integrate the dataset recorded during nighttime overpasses (cf., Tables 2 and 3).

Figure 4

2.5. Volcanic Radiative Power

When a pixels is flagged as *alert*, the “above background” at 4μm radiance (ΔL_{4PIX}) is calculated as:

$$\Delta L_{4PIX} = L_{4alert} - L_{4bk} \quad (4)$$

where L_{4alert} is the 4 μm radiance of the alerted pixel/s and L_{4bk} is the background radiance at 4μm. This last, L_{4bk}, it is estimated from the arithmetic mean of all the pixels surrounding the alerted one (or around the alerted cluster) not contaminated by clouds. Accordingly, cloudy pixels were detected using the method described by Giglio et al., (2003) so that:

cloud= [BT_{11}<255] [Condition 4; for nighttime data]

or

cloud= [(R_1+R_2)>0.9] or [BT_{11}<245] or [((R_1+R_2)>0.9) & (BT_{11}<265)] [Condition 5; for daytime data]

where BT_{11} is the brightness temperature (in K) of band 11 (retrieved from L_{11} using the Plank’s function), and R_1 and R_2 are the reflectivity of bands 1 and 2, respectively.

Following Wooster, Zhukov, and Oertel (2003), we calculated the Volcanic Radiative Power (*VRP* in W) by means of the MIR method. Hence, for any individual alerted pixels, the VRP_{PIX} is calculated as:

$$VRP_{PIX} = 18.9 \times A_{PIX} \times \Delta L_{4PIX} \quad (5)$$

where A_{PIX} is the pixel size (1 km^2 for the resampled MODIS pixels).
When two or more pixels (a cluster of pixels) are alerted, the total radiative power is finally calculated as the sum of the single VRP_{PIX}, so that:

$$VRP = \sum_{1}^{nalert} VRP_{PIX} \quad (6)$$

where *nalert* is the number of alerted pixels.

3. Algorithm performance

Due to the differences of the nighttime and daytime alert detection procedures, the two algorithms must be considered separately when testing their performances.
To test the performance of the nighttime algorithm, we followed the methodology of Steffke and Harris (2011) and we visually inspected all the *NTI* images in order to identify the presence of a real hotspot ("Manual" alerts, Table 2). These hand-picked images were used as a reference benchmark for comparing these results with those obtained by using the algorithm (see algorithm alerts in Table 2). This is computed in terms of how many automatic detections are effectively consistent with those manually identified (cf. "Correct" in Table 2). Hence, the difference between the "Manual" and the "Correct" detections represents the "Missed" detections (Table 2). Finally, when

the algorithm detected a hotspot that was not validated by visual inspection, we classified it as a "False" detection (cf. Table 2).

The results of this comparison, are shown in Table 2 where the total number of detections (and their relative percentage), are subdivided year by year. In addition, in Figure 5 we also show a typical NTI map for each detection case (Correct, Missed and False detections).

Figure 5

The overall comparison suggests that the nighttime algorithm perform correctly on ~79% of the "Manual" detections, with ~22% of "Missed" cases, and less than 4% of "False" alerts (Table 2). Noticeably, all the "False" detections consist of small amplitude thermal anomalies (i.e. *VRP* < 2 MW), and they could be easily eliminated by setting a cutoff at 2 MW. However, such a cutoff will also produce a strong reduction of the efficiency of the algorithm, with the "Correct" detections decreasing from ~79% to less than 59%. Since most of the "False" detections are low-amplitude ones, we preferred to keep some false alerts than missing several real hotspots.

The excellent performance of the nighttime algorithm is also evident by means of comparing the frequency of alerted detections retrieved both manually ($f_{alertManual} = N_{alert,Manual}/N_{Overpasses}$) and automatically ($f_{alert,algorithm} = N_{alert,,algorithm}/N_{Overpasses}$) (Figure 6*(a)*). The best linear fit plots close to the 1:1 ratio (with R^2= 0.97), thus suggesting an excellent agreement over the whole range of f_{alert}. However, the percentage of "Correct" detections seems to be affected by the level of volcanic activity (Figure 6*(b)*), which is basically correlated with the frequency of detection ($f_{alert,algorithm}$). This means that the algorithm is most highly efficient during effusive phases, whereas it reduces its performance during periods of weak to moderate strombolian activity. From Table 2 it also appear that the number of "False" detection it is not correlated with the level of activity and remain typically around four cases per year.

Figure 6

The overall effectiveness of the nighttime algorithm can be finally compared with the results obtained by Coppola et al., (2012) which analyzed nighttime MODIS data at Stromboli volcano between 2000 and 2012 with a different algorithm. In our previous paper (Coppola et al., 2012) we found 743 alerts during 9635 overpasses, with an average frequency of alert detection ($f_{alert}=N_{alert}/N_{Overpasses}$) equal to 8.5%. Over the same period the new algorithm (section 2.4.1) detected 1332 alerts (f_{alert}=15%; Table 2), thus doubling the detection capability (particularly for small-amplitude thermal anomalies) with respect to our previous alghorithm (Coppola et al., 2012). For comparison, during 2000-2012 the MODVOLC system (which use a simple fixed threshold) detected at Stromboli volcano 442 nighttime alerts (f_{alert}=4.5%), half of which identified during the effusive periods of activity.

Figure 7

Testing the performance of the daytime algorithm is more problematic, due to the difficulty in discriminating “false” and “real” hotspot using the visual inspection of each image. As previously discussed, this difficulty relies on solar heating effects, so that discriminating a genuine volcanic hot-spot from a pixel “naturally” hotter than its surrounding is rather challenging. This is particularly true for low-amplitude thermal anomalies, whose radiance in the MIR channel may exceed only moderately from their background values. Therefore, there are no effective benchmarks for testing the daytime algorithm despite visual data inspection. However, this procedure it is useful to exclude by eye the presence of evident “False” detections.

An alternative approach to evaluate the daytime algorithm takes into account the nighttime detections as a reference thermal signal. We thus plotted separately the *VRP* retrieved from nighttime and daytime data (Figure 7). In particular, we compared the results for a period of high thermal emissions (the first seven months of 2003 effusive activity; Figure 7*(a)*) with those obtained for a year of lower thermal emissions (characterized by low to mild strombolian activity during 2009; Figure 7*(b)*). In both the cases, the trends of thermal outputs confirm an excellent agreement between the two dataset (daytime and nighttime). Notably, during the effusive phase the daytime algorithm performed very well in terms of mean *VRP* (the average value of the *VRP* measurements) as well as in tracking the general trend of the eruptive sequence (Figure 7*(a)*). However, the number of daytime detections was almost halved with respect to the nighttime detections, likely due to the minor efficiency of the algorithm in detecting small thermal anomalies.

The minor sensitivity of the daytime algorithm is also evident by comparing the dataset recorded during one year of typical strombolian activity (i.e. during 2009; Figure 7*(b)*). The general trend of daytime data is still consistent with the fluctuations of thermal outputs recorded during the night. However, the number of alert detections obtained by applying the daytime algorithm drastically decreased. Again these results demonstrate the limits of the daytime algorithm which is unable to detect smaller hotspots. In fact the daytime dataset consist of 364 alerts over a total of 9599 overpasses, which gives a mean f_{alert} equal to 4% (Table 3). This compares with a frequency of alert detection of 15% for nighttime images thus enhancing the different efficiency in hotspot detection of the two algorithms.

4. Statistical analysis of VRP and thermal regimes

We here focus our analysis on the nighttime dataset for statistical reasons. This dataset consists of a large number of observations (1445 data) and shows a higher efficiency in detecting small thermal anomalies.

As a whole, the entire nighttime dataset indicates that *VRP* is ranging from < 1 MW to more than 3000 MW, thus spanning over three orders of magnitude. Particularly, its frequency distribution is extremely peaked and skewed toward higher values, as shown in Figure 8*(a)*. A useful way to visualise the shape and properties of such kind of positive, asymmetric distributions consists in transforming the original data (*VRP*) into log-transformed data (log[*VRP*]). This procedure was previously used to identify distinct thermal regimes at Stromboli and Nyamuragira volcanoes (Coppola et al., 2012; 2013).

Our new dataset for Stromboli volcano (log(*VRP*) records) reveals the presence of two main regimes that intersect around 30 MW (*logVRP*=7.5; Figure 8*(b)*). Similarly, Coppola et al., (2012) found that a VRP of ~50 MW marks a change in the eruptive style of Stromboli, basically identified with the transition from strombolian-dominated to effusive-dominated activity. The small discrepancy between the two thresholds is likely due to the higher sensibility of the new algorithm which is able to detect a larger number of small thermal anomalies (see chapter 3). However our analysis remains consistent with those previously provided by Coppola et al. (2012) and confirm the presence, at Stromboli volcano, of two main thermal regimes (strombolian and effusive) overlapping at 30-50 MW.

Considering the modal value of each regime (the most frequent value), we here estimate that strombolian and effusive activities are characterised by a typical *VRP* of 4 MW (*logVRP*=6.6) and 100 MW (*logVRP*=8), respectively. Based on this simple relation we may roughly infer that the energy radiated during twenty-five years of strombolian activity is almost equivalent to those realised during one year of effusive activity.

Figure 8

A deeper investigation on the *VRP* distribution can be achieved by plotting the log-transformed data (*log(VRP)*) within a normal probability plot (Figure 9). Here, a population of events (or observations) log-normally distributed follows a straight line, as showed by the black dashed line (Figure 8). Though the most of the dataset follows approximately this kind of distribution we suggest that some minor inflection points, separating groups of data, may be regarded as changing points indicative of distinct radiating regimes. The inferred inflection points appears around 1, 15, 80, 315 and 1000 MW and defines six main radiating regimes hereby named Very Low, Low, Moderate, High, Very High and Extreme (Figure 9).

Figure 9

The "Very Low" radiating regime (*VRP* < 1 MW) represents about 17 % of the data and includes essentially the most of the false alerts detected by the algorithm. However, in the 75% of the cases the detection of a Very Low regime represents a genuine hotspot which may be associated to the presence of a single vent (with a radius of ~ 1 m and temperature of 950°C) within the summit area of Stromboli.

The "Low" radiating regime (1 MW < *VRP* < 15 MW) is the most represented group, comprising more than 55% of the data. This regime consist of the bulk thermal emissions associated to the "typical" strombolian activity typically characterized by persistent degassing and frequent explosive events occurring at one to 15 open vents (Harris and Stevenson, 1997).

This regime gradually shifts toward the "Moderate" radiating regime (15 MW < *VRP* < 80 MW) that is represented by about 15% of the data. The "Moderate" regime is typical of periods with more vigorous strombolian activity which may evolve into short periods of sustained spattering and/or fountaining or eventually summit overflows (Coppola et al., 2012). We regard the "Moderate" regime as a transitional state (between strombolian and effusive) characterised by the uprising of the magma column that is feeding the active vents. Eventually this regime may prelude the transition into a pure effusive phase (flank eruption) as observed before the 2002-2003 and 2007 eruptions (Coppola et al., 2012).

The transition from "Moderate" to "High" thermal regimes marks a clear change in the eruptive style of Stromboli, leading to lava effusion (Figures 9). The "High" radiating regime (80 MW < *VRP* < 315 MW) is represented by 10% of the data and it has been observed during the second phase of the 2002-2003 eruption (from mid-February 2003 to July 2003) as well as during the most of the summit overflows recently occurred at Stromboli (Coppola et al., 2012). Notably, during these periods the effusion of lava typically occurred at a rates < $1 m^3 s^{-1}$ (Calvari et al., 2005, Ripepe et al., 2005, INGV Report 2011-08-02).

Conversely, the "Very High" radiating regimes (315 MW < *VRP* < 1000 MW) has been recorded during the initial phases of the 2002-2003 major eruption (from January to mid-February 2003), as well as during the 2007 eruption and some major, long-lived overflows (such as those of December 2012 (Figure 9). The "Very High" regime includes only 2% of the observations and it is always associated with sustained lava effusion with a discharge rates of 1 to 5 $m^3 s^{-1}$ (Marsella et al., 2009; Calvari et al., 2010).

Finally, the highest thermal regime (hereby defined as "Extreme"; *VRP* > 1000 MW) has been recorded only two times during the last fourteen years on 28 December 2002 and on 27 February 2007 (Figure 9). In particular, these cases, that represents only 0.1% of the data, where recorded few hours after the beginning of the two major flank eruptions and marks the onset of the main effusive phases. In these cases, lava discharge rate were higher than 10 $m^3 s^{-1}$ (Calvari et al., 2005; Neri and Lanzafame, 2008), and accompanied the initial and very fast emplacement of lava flows along the "Sciara del Fuoco". We thus infer that the detection of such high *VRP* (>1000 MW) likely indicates the onset of a flank eruption at Stromboli volcano. A complete timeseries of VRP recorded between 2000 and 2012 (nighttime data only) is shown in Figure 10 where the colour of each detection (stem) is function of the ongoing thermal regime.

Figure 10

5. Discussion

Coppola et al., (2012) reported that all the detection above 50 MW were coeval with major episodes of spattering and lava overflows. However, the whole cross validation of the thermal activity levels described above is challenging due to limited field observations and related reports. To overcome these problems and to better understand the thermal regimes and their bearings with volcanic activity levels, it is worth to compare thermal MODIS outputs with the explosive levels recorded (on a daily basis since 2005) by the Laboratorio di Geofisica Sperimentale of the University of Florence (cf., http://lgs.geo.unifi.it/) and sent to the Italian Civil Protection Department (DPC). The explosive level is based on a data set of geophysical parameters (seismic, infrasound, number of explosions, deformation) recorded for over a decade: it is subdivided into five levels, representing an average assessment of the explosive intensity (i.e., 0 - Not determined; 1 – Low; 2 – Moderate; 3 – High; 4 – Very high). The timeseries reported in Figure 11, indicates an overall correlation between thermal and explosive levels (such as their averages on a weekly basis), with a general increase of the thermal output during periods characterised by high explosive activity.

Figure 11

However, this comparison also suggests that different periods, or different types of activity show rather peculiar links between thermal and explosive levels. This is particularly evident by plotting the explosive levels vs. the thermal levels, as shown in Figure 12. Here, several distinct fields may be visualised: each one of them characterises a specific type of volcanic activity or eruptive period. For instance, the onset of the 2007 effusive eruption was characterized by an “extreme” thermal level, associated to a “very high” explosive level (star in Figure 12). Conversely, the subsequent flank effusion was characterised by very high thermal levels coeval with a low explosive activity (red circles). This particular relationship was likely due to the sharp ceasing of the explosive activity at summit vents, due to the propagation of an effusive fracture down to the central part of NE flank; this event drained the lava out of the crater area and was followed by a sharp decrease in geophysical and geochemical parameters (e.g., Ripepe et al., 2009; Cigolini et al., 2013). An additional case is given by the major summit overflows that occurred between 2008 and 2012 (black arrows in Figure 11). Here, the high thermal levels were associated to a moderate-high explosive activity (black circles), thus suggesting that summit outflows were accompanied to a sustained explosive activity. Finally, the dataset suggests that the ratio between thermal and explosive levels were somehow different during the 2005-2006 and the 2008-2012 eruptive periods (blue and pink circles, respectively): after the 2007 eruption the thermal to explosive ratio was generally higher than before the eruption, thus suggesting that some changes occurred in the eruptive dynamics.

Figure 12

6. Conclusions

We have developed a new algorithm which is specifically addressed to the detection of small hot spot associated with thermal anomalies typical of strombolian activity. In particular, the new algorithm was developed on the basis of the constant position of thermal anomalies that substantially coincides with the active summit vents. Moreover, it includes principles of contextual, temporal and spectral hot spot detection approaches/methods. The application of this algorithm in analyzing Stromboli activity is very efficient (up to 95 % of correct alerts) and reduces the rate of false alerts (typically around four per year), especially when applied to nighttime data. The high efficiency in tracking small hot spot (< 1 MW), coupled with the analysis of MODIS derived thermal records for over a decade, gave us the opportunity to build up an exhaustive dataset of volcanic radiative power (*VRP*) measurements. Notably, the frequency distribution and the probability plot of these thermal records allows the definition of distinct radiating regimes which are closely associated to different levels of volcanic activity. We thus suggest that the refinement of a near real time processing scheme allow us to discriminate, on the basis of satellite-based thermal monitoring, the changes in strombolian activity: such as, for instance, the occurrence of summit overflows as well as the possible onset of lateral flank eruptions. Finally, we trust that a wise comparison of the retrieved thermal outputs with other geophysical and geochemical parameters, is an additional key-factor for better understanding the eruptive dynamics at Stromboli. However, similar approaches could be taken in monitoring other persistently active volcanoes.

Acknowledgments

This research has benefited from funding provided by the Italian Presidenza del Consiglio dei Ministri - Dipartimento della Protezione Civile (DPC) as part of the DEVnet Programme that includes a collaborative project between the Departments of Earth Sciences of the University of Florence and the University of Torino. Scientific papers funded by DPC do not represent its official opinion and policies.

We acknowledge the NASA-LAADS (http://ladsweb.nascom.nasa.gov/) for providing the complete archive of level 1b MODIS data and the LANCE-MODIS system (http://lance-modis.eosdis.nasa.gov/) for maintaining and delivering Near Real Time MODIS products. The manuscript has been improved by the critical comments and suggestions of two anonymous reviewers.

References

Barberi, F., M. Rosi, and A. Sodi, 1993. "Volcanic hazard assessment at Stromboli based on review of historical data." *Acta Vulcanologica* 3: 173-187.

Calvari, S., L. Spampinato, L. Lodato, A. J. L. Harris, M. R. Patrick, J. Dehn, M. R. Burton, and D. Andronico, 2005. "Chronology and complex volcanic processes during the 2002–2003 flank eruption at Stromboli volcano (Italy) reconstructed from direct observations and surveys with a handheld thermal camera." *Journal of Geophysical Research* 110(B02201). doi:10.1029/2004JB003129.

Calvari, S., L. Lodato, A. Steffke, A. Cristaldi, A. J. L. Harris, L. Spampinato, and E. Boschi, 2010. "The 2007 Stromboli flank eruption: chronology of the events, and effusion rate measurements from thermal images and satellite data." *Journal of Geophysical Research* 115(B4): B04201. doi:10.1029/2009JB006478.

Cigolini, C., M. Laiolo, G. Ulivieri, D. Coppola, and M. Ripepe, 2013. "Radon Mapping, automatic measurements and extermely high 222Rn emissions during the 2002-2007 eruptive scenarios at Stromboli volcano." *Journal of Volcanology and Geothermal Research* 264: 49–65.

Coppola, D., D. Piscopo, M. Laiolo, C. Cigolini, D. Delle Donne, and M. Ripepe, 2012. "Radiative heat power at Stromboli volcano during 2000–2011: twelve years of MODIS observations." *Journal of Volcanology and Geothermal Research* 215–216: 48–60.

Coppola, D., M. Laiolo, D. Piscopo, and C. Cigolini, **2013.** "Rheological control on the radiant density of active lava flows and domes." *Journal of Volcanology and Geothermal Research* 249: 39–48, doi: 10.1016/j.jvolgeores.2012.09.005.

Coppola, D., C. Cigolini, **2013**. "Thermal regimes and effusive trends at Nyamuragira volcano (DRC) from MODIS infrared data." *Bulletin of Volcanology* (submitted).

Dean, K.G., M. Servilla, A. Roach, B. Foster, and K. Engle, 1998. "Satellite monitoring of remote volcanoes improves study efforts in Alaska." *EOS Transactions* 79(413): 422–423.

Dehn, J., K. G. Dean, and K. Engle, 2000. "Thermal monitoring of North Pacific volcanoes from space." *Geology* 28(8): 755–758

Di Bello, G., C. Filizzola, T. Lacava, F. Marchese, N. Pergola, C. Pietrapertosa, S. Piscitelli, I. Scaffidi, and V. Tramutoli, 2004. "Robust satellite technique for volanic and seismic hazard monitoring." *Annals of Geophysics* 47(1): 49–64

Flynn, L. P., R. Wright, H. Garbeil, A. J. L. Harris, and E. Pilger, 2002. “A global thermal alert using MODIS: initial results from 2000–2001.” *Advances in Environmental Monitoring and Modeling*, 1: 5-36.

Galindo, I., and T. Dominguez, 2002. “Near real-time satellite monitoring during the 1997–2000 activity of Volcan de Colima (Mexico) and its relationship with seismic monitoring.” *Journal of Volcanology and Geothermal Research* 117: 91–104.

Ganci, G., A. Vicari, L. Fortuna, and C. Del Negro, 2011. “The HOTSAT volcano monitoring system based on combined use of SEVIRI and MODIS multispectral data.” *Annals of Geophysics* 54: 544-550.

Ganci, G., A. Vicari, A. Cappello, and C. Del Negro, 2012. “An emergent strategy for volcano hazard assesement: From thermal satellite monitoring to lava flow modelling.” *Remote Sensing of Environments* 119: 197-207.

Giglio, L., J. Descloitresa, C. O. Justicec, and Y. J. Kaufman, 2003. “An enhanced contextual fire detection algorithm for MODIS.” *Remote Sensing of Environments* 87: 273–282.

Harris, A. J. L., D.A. Rothery, R. W. Carlton, S. Langaas, and H. Mannstein, 1995. “Non-zero saturation of AVHRR thermal channels over high temperature targets: evidence from volcano data and a possible explanation.” *International Journal of Remote Sensing* 16(1): 189–196.

Harris, A. J. L., L. Keszthelyi, L. P. Flynn, P. J. Mouginis-Mark, C. Thornber, J. Kauahikaua, D. Sherrod, F. Trusdell, M. W. Sawyer, and P. Flament, 1997. “Chronology of the Episode 54 eruption at Kilauea Volcano, Hawaii, from GOES-9 satellite data.” *Geophysical Research Letters* 24(24): 3281–3284.

Harris, A. J. L., and D. S. Stevenson, 1997. “Thermal observations of degassing open conduits and fumaroles at Stromboli and Vulcano using remotely sensed data.” *Journal of Volcanology and Geothermal Research* 76: 175–198.

Harris, A. J. L., E. Pilger, H. Garbeil, P. J. Mouginis-Mark, J. Kauahikaua, C. Thornber, 2001. "Automated, high temporal resolution, thermal analysis of Kilauea volcano, Hawaii, using GOES-9 satellite data." *International Journal of Remote Sensing* 22(6): 947–967.

Harris, A. J. L., E. Pilger, and L. P. Flynn, 2002. "Web-based hot spot monitoring using GOES: what it is and how it works." *Advances in Environmental Monitoring and Modeling* 1(3): 134–151.

Higgins, J., and A. J. L. Harris, 1997. "VAST: a program to locate and analyse volcanic thermal anomalies automatically from remotely sensed data." *Computer and Geosciences* 23(6): 627–645.

Hirn, B., C. Di Bartola, and F. Ferrucci, 2009. "Combined use of SEVIRI and MODIS for detecting, measuring, and monitoring active lava flows at erupting volcanoes." *IEEE Transactions on Geoscience and Remote Sensing* 47: 2923-2939.

INGV Report, 2011. "In Rapporti di Vulcanologia: Sopralluogo a Stromboli del 2 agosto 2011." Available at http://www.ct.ingv.it/ 2011.

Kaneko, T., A. Yasuda, T. Ishimaru, M. Takagi, M. J. Wooster, T. Kagiyama, 2002. "Satellite hot spot monitoring of Japanese volcanoes: a prototype AVHRR-based System." *Advances in Environmental Monitoring and Modeling* 1(1): 125–133.

Kervyn, M., A. J. L. Harris, E. Mbede, F. Belton, P. Jacobs, and G. G. J. Ernst, 2006. "MODLEN: A semi-automated algorithm for monitoring small scale thermal activity at Oldoinyo Lengai Volcano Tanzania." In: *Quantitative Geology from Multiple Sources*, IAMG Ann Conf. Liege.

Koeppen, W. C., E. Pilger, and R. Wright, 2011. "Time series analysis of low resolution thermal infrared thermal anomalies: a hybrid approach." *Bulletin of Volcanology* 73: 577–593. doi 10.1007/s00445-010-0427-y.

Laiolo, M., C. Cigolini, D. Coppola, and D., Piscopo, 2012. "Developments in real-time radon monitoring at Stromboli volcano." *J. Environm. Radioactivity* 105: 21-29.

Marsella, M., C. Proietti, A. Sonnessa, M. Coltelli, P. Tommasi, and E. Bernardo, 2009. "The evolution of the Sciara del Fuoco subaerial slope during the 2007 Stromboli eruption: relation between deformation processes and effusive activity." *Journal of Volcanology and Geothermal Research* 182(3–4): 201–213.

Neri, M., and A. Lanzafame, 2008. "Structural features of the 2007 Stromboli eruption." *Journal of Volcanology and Geothermal Research* 182(3–4): 137–144.

Newhall, C. G., and S. Self, 1982. "The volcanic explosivity index (VEI): An estimate of explosive magnitude for historical volcanism." *Journal of Geophysical Research* 87: 1231-1238.

Nishihama, M., R. E. Wolfe, D. Solomon, F. S. Patt, J. Blanchette, A. J. Fleig, and E. Masuoka, 1997. "MODIS Level 1A Earth Location Algorithm Theoretical Basis Document Version 3.0." SDST-092. Lab Terrestrial Phys NASA Goddard Space Flight Center, Greenbelt, MD.

Pergola, N., F. Marchese, V. Tramutoli, 2004. "Automated detection of thermal features of active volcanoes by means of infrared AVHRR records." *Remote Sensing of Environments* 93: 311–327.

Ramsey, M. S., and A. J. L. Harris, 2013. "Volcanology 2020: How will thermal remote sensing of volcanic surface activity evolve over the next decade?" *Journal of Volcanology and Geothermal Research* 249: 217-233.

Ripepe, M., E. Marchetti, G. Ulivieri, A. J. L. Harris, J. Dehn, M. R. Burton, T. Caltabiano, and G. Salerno, 2005. "Effusive to explosive transition during the 2003 eruption Stromboli volcano." *Geology* 33(5): 341–344.

Ripepe, M., D. Delle Donne, G. Lacanna, E. Marchetti, G. Ulivieri, 2009. "The onset of the 2007 Stromboli effusive eruption recorded by an integrated geophysical network. *Journal of Volcanology and Geothermal Research* 182: 131-136.

Rosi, M., A. Bertagnini, and P. Landi, 2000. "Onset of persisting activity at Stromboli Volcano (Italy)." *Bulletin of Volcanology* 62: 294-300.

Steffke, A. M., and A. J. L. Harris, 2011. "A review of algorithms for detecting volcanic hot spots in satellite infrared data." *Bulletin of Volcanology* 73:1109–1137. doi 10.1007/s00445-011-0487-7.

Toller, G. N., A. Isaacman, and J. Kuyper, 2006. "MODIS Level 1B Product User's Guide." Prepared by Members of the MODIS Characterization Support Team For NASA/Goddard Space Flight Center Greenbelt, MD 20771.

Webley, P. W., M. J. Wooster, W. Strauch, J. A. Saballos, K. Dill, P. Stephenson, J. Stephenson, R. Escobar Wolf, and O. Matias, 2008. "Experiences from real-time satellite-based volcano monitoring in Central America: case studies at Fuego, Guatemala." *International Journal of Remote Sensing* 29(22): 6618–6644.

Wooster, M. J., B. Zhukov, and D. Oertel, 2003. "Fire radiative energy for quantitative study of biomass burning: derivation from the BIRD experimental satellite and comparison to MODIS fire products." *Remote Sensing of Environments* 86: 83–107.

Wright, R., L. P. Flynn, H. Garbeil, A. J. L. Harris, and E. Pilger, 2002. "Automated volcanic eruption detection using MODIS." *Remote Sensing of Environments* 82: 135–155.

Wright, R., and L. P. Flynn, 2004. "Space-based estimate of volcanic heat flux into the atmosphere during 2001 and 2002." *Geology* 32(3): 189–192.

Wright, R., L. P. Flynn, H. Garbeil, A. J. L. Harris, and E. Pilger, 2004. "MODVOLC: near-real-time thermal monitoring of global volcanism." *Journal of Volcanology and Geothermal Research* 135: 29–49.

Wright, R., L. Glaze, S. M. Baloga, 2011. "Constraints on determining the eruption style and composition of terrestrial lavas from space". *Geology* 39: 1127-1130.

Appendix 1

List of parameters and specific definitions used in the algorithm

Parameter	Definition	Explanation
ROIs	Region of Inerest (s=1,2 or 3)	
NTI	Normalised Thermal Index	Equation 1 applied pixel per pixel on nighttime images
NTI_{corr}	Normalised Thermal Index corrected for solar reflection	Equation 3 applied pixel per pixel on daytime images
NTI_{ROIs}	NTI of pixels within ROIs	Equation 1 applied to the pixels of ROIs
NTI_{Ref2}	Reference pixels of ROI2	Pixels of ROI2 satisfiyng Condition 2
NTI_{Max2}	Maximum NTI of NTI_{Ref2}	
NTI_{Mean2}	Mean NTI of NTI_{Ref2}	
NTI_{Std2}	Standard deviation of NTI_{Ref2}	
NTI_{thres1}	Empirical upper NTI threshold (nighttime algorithm)	Equation 2 with parameters settled in Table 1
NTI_{thres2}	Empirical lower NTI threshold (nighttime algorithm)	Equation 2 with parameters settled in Table 1
NTI_{thres3}	Empirical upper NTI threshold (daytime algorithm)	Equation 2 with parameters settled in Table 1
Alert1	Alerted pixel(s)	Pixel(s) flagged as "alert" using Test 1 (nighttime algorithm)
Alert2	Alerted pixel(s)	Pixel(s) flagged as "alert" using Test 2 (nighttime algorithm)
Alert3	Alerted pixel(s)	Pixel(s) flagged as "alert" using Test 3 (daytime algorithm)
cloud	Cloudy pixel(s)	Pixel(s) considered as "cloudy" using Conditions 3 and 4
L_{4alert}	MIR radiance (at 4mm) of alerted pixel(s)	
L_{4bk}	Backgound MIR radiance (at 4mm) of alerted pixel(s)	arithmetic mean of all the pixels surrounding the alerted one (or around the alerted cluster) not contaminated by clouds
ΔL_{4PIX}	"Above background" MIR radiance of alerted pixel(s)	Equation 4
VRP_{PIX}	Volcanic Radiative Power of alerted pixel(s)	Equation 5

Tables

TABLE 1 - Parameters used to define the NTI thresholds (Equation 2)

Parameter	Unit	$NTI_{Thresh1}$	$NTI_{Thresh2}$	$NTI_{Thresh3}$
A [NTI variation]	adimensional	0.02	0.02	0.07
P [cycle length]	day^{-1}	π/183	π/183	π/183
α [phase shift]	day	121	121	106
C [NTI baseline]	adimensional	-0.865	-0.915	-0.82

TABLE 2 - Summary of the nighttime alerts detected manually ("Manual") and automatically by the algorithm

Year	Overpasses	Manual[a]	Algorithm[a]			
				Correct[1]	Missed[1]	False[2]
	no.	no. *(%)*	no. *(%)*	no. *(%)*	no. *(%)*	no. *(%)*
2000	339	37 *(10.9)*	32 *(9.4)*	25 *(67.6)*	12 *(32.4)*	7 *(21.8)*
2001	406	14 *(3.4)*	16 *(3.9)*	10 *(71.4)*	4 *(28.6)*	6 *(37.5)*
2002	597	72 *(12.1)*	54 *(9.0)*	50 *(69.4)*	22 *(30.6)*	4 *(7.4)*
2003	818	386 *(47.2)*	370 *(45.2)*	364 *(94.3)*	22 *(5.7)*	6 *(1.6)*
2004	833	77 *(9.2)*	46 *(5.5)*	45 *(58.4)*	32 *(41.6)*	1 *(2.2)*
2005	836	70 *(8.4)*	43 *(5.1)*	39 *(55.7)*	31 *(44.3)*	4 *(9.3)*
2006	819	124 *(15.1)*	99 *(12.1)*	91 *(73.4)*	33 *(26.6)*	8 *(8.1)*
2007	822	197 *(24.0)*	179 *(21.8)*	175 *(88.8)*	22 *(11.2)*	4 *(2.2)*
2008	827	166 *(20.1)*	127 *(15.4)*	125 *(75.3)*	41 *(24.7)*	2 *(1.6)*
2009	835	199 *(23.8)*	140 *(16.8)*	140 *(70.3)*	59 *(29.6)*	0 *(0.00)*
2010	836	103 *(12.3)*	84 *(10.0)*	83 *(80.6)*	20 *(19.4)*	1 *(1.2)*
2011	837	179 *(21.4)*	142 *(17.0)*	138 *(77.1)*	41 *(22.9)*	4 *(2.8)*
2012	830	155 *(18.7)*	113 *(13.6)*	110 *(71.0)*	45 *(29.0)*	3 *(2.6)*
TOTAL	9635	1779 *(18.5)*	1445 *(15.0)*	1395 *(78.4)*	384 *(21.6)*	50 *(3.5)*

a - percentages are calculated as the number of detections over the number of the overpasses

1 - percentages are calculated from the fraction of "Correct" and "Missed" detections, with respect to the "Manual" detections

2 - percentages are calculated from the fraction of "False" detections with respect to the “Algorithm” detections

TABLE 3 - Summary of daytime thermal alerts detected by the algorithm

Year	Overpasses	Algorithm	
	no.	no.	*%*[a]
2000	320	3	*0.9%*
2001	397	2	*0.5%*
2002	574	13	*2.3%*
2003	809	172	*21.3%*
2004	813	11	*1.4%*
2005	842	5	*0.6%*
2006	830	11	*1.3%*
2007	836	48	*5.7%*
2008	842	11	*1.3%*
2009	848	27	*3.2%*
2010	821	15	*1.8%*
2011	823	28	*3.4%*
2012	844	18	*2.1%*
TOTAL	9599	364	*3.8%*

a - percentages are calculated as the number of detections over the number of the overpasses

Figure Captions

Figure 1. Location of Stromboli volcano in the Southern Tyrrhenian sea,

Figure 2. *(a)* Example of *NTI* Map obtained from nighttime images (acquired on June 16, 2006 over Stromboli). Note the thermal anomalous pixels (bright pixels) over the summit of the volcano; *(b)* Regions of Interest (ROIs) defined for the hot-spot detection scheme (see text for explanation).

Figure 3. *(a) NTI* time-series for the 2006 nighttime data over Stromboli. Each point represents the *NTI* of a single pixel. Different colors refer to the three distinct ROIs (see the electronic text for the colors). The two sinusoidal lines envelop the fluctuations of the *NTI* due to the seasonal trend; *(b)* The same NTI time-series with the alerts detected by the algorithm overlapped. *Alert1* and *Alert2* are obtained using the Test 1 and 2 respectively (see the text for explanation). For colors refer to the electronic copy.

Figure 4. *(a) NTI* time-series relative to the 2006 daytime data over Stromboli. Each point represent the *NTI* of a pixel. The different colors refers to the three distinct ROIs (see the electronic version for the colors); *(b)* the *NTI* timeseries corrected for solar reflection according to the Equation (3). The alerts detected by the daytime algorithm (obtained using the Test 3) are overlapped. For colors refer to the electronic copy.

Figure 5. *(a)* Zoomed view of selected nighttime *NTI* map (ROI2 and ROI3 only) recorded on February 12, 2006; any anomaly is visible over Stromboli volcano and the island appears cooler than the surrounding area. Three other examples of nighttime NTI maps represent the following

cases: Correct *(b)*, Missed *(c)* and False *(d)* detections (resulting from the nighttime algorithm). The squares marks the location of the Correct (red), Missed (blue) and False (white) pixels. For colors refer to the electronic copy.

Figure 6. *(a)* Relationship between the frequency of alert detection retrieved manually ($f_{alertManual}$) and automatically ($f_{alert,algorithm}$); *(b)* percentage of "Correct" detection as a function of $f_{alert,algorithm}$. The algorithm performs almost optimally during period characterized by $f_{alert,algorithm}$ >0.5.

Figure 7. *(a)* Comparison of thermal outputs during 2003 (a) and 2009; *(b)* the nighttime algorithm (blue) and the daytime algorithm (red) are reported. For colors refer to the electronic copy.

Figure 8. *(a)* Frequency histogram of *VRP* data recorded during 2000-2013 (nighttime only); *(b)* frequency histogram of log-transformed data (*logVRP*) enhancing the presence of two main regimes associated to the strombolian and effusive activity, respectively. These two regimes intersect at about 30 MW (*logVRP*=7.5).

Figure 9. Probability plot of *logVRP*. Black dashed line represent the best fit regression by assuming a pure lognormal distribution. The vertical lines represent the inferred inflection points used to define 6 distinct thermal regimes: very low, low, moderate, high, very high and extreme thermal outputs. Note that the two *VRP* recorded during the onset of the effusive flank eruption (violet stars) are the only "extreme" values detected between 2000 and 2013. The threshold of 30 MW is in the middle of the Moderate regime, which is ascribed to the transition between strombolian-dominated and effusive-dominated activity, respectively. For colors refer to the electronic copy.

Figure 10. *VRP* timeseries (on log scale) recorded at Stromboli between 2000 and 2013. Different colours refer to the thermal regimes previously defined (see the text for explanation). The red horizontal line is the threshold at 30 MW separating the strombolian activity from lava effusion. For colors refer to the electronic copy.

Figure 11. Thermal activity levels (left axis; red line) and explosive levels (right axis; gray bars) recorded between 2005 and 2012. The different colour scales on the two axes refer to thermal regimes (obtained by MODIS, left hand-side) and explosive regimes (right hand-side, evaluated by the Laboratorio di Geofisica Sperimentale of University of Florence; http://lgs.geo.unifi.it/) based on multiparametric recordings (seismic, infrasonic, number of explosions, deformation). The black arrows indicate the timing of major overflows. The occurrence of the February 2007 eruption is marked by a sharp increase in thermal levels coeval with a decrease in explosive activity. For colours refer to the electronic copy.

Figure 12. Scatter-plot of explosive vs. thermal levels of activity recorded at Stromboli between 2005 and 2012. Note how different kind of activities (such us eruption onset, effusive flank eruption, major overflows, etc.) fall within different fields (see text for details). For colours refer to the electronic copy.

Fig. 1

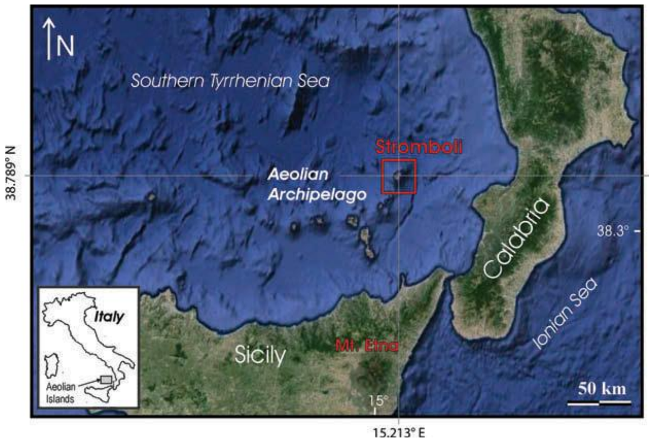

Fig. 2

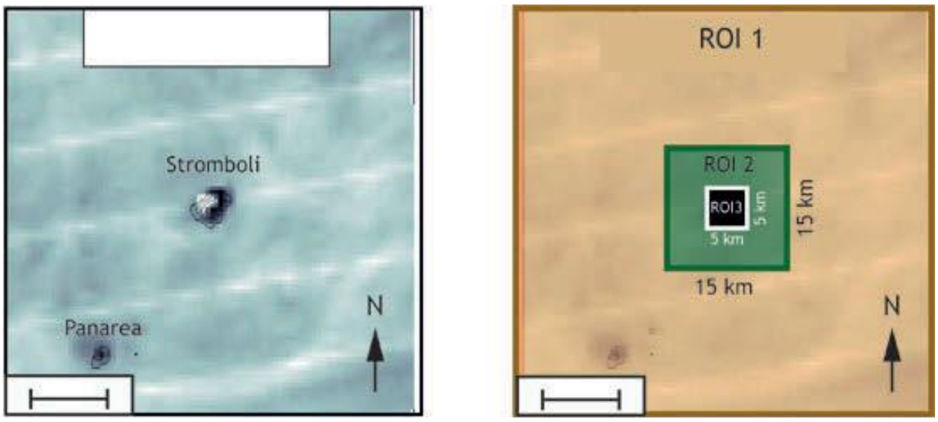

Fig. 3

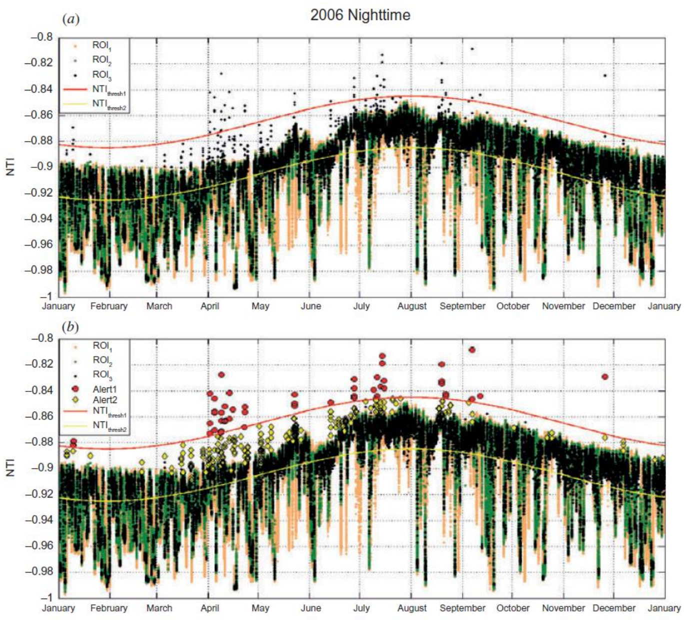

Fig. 4

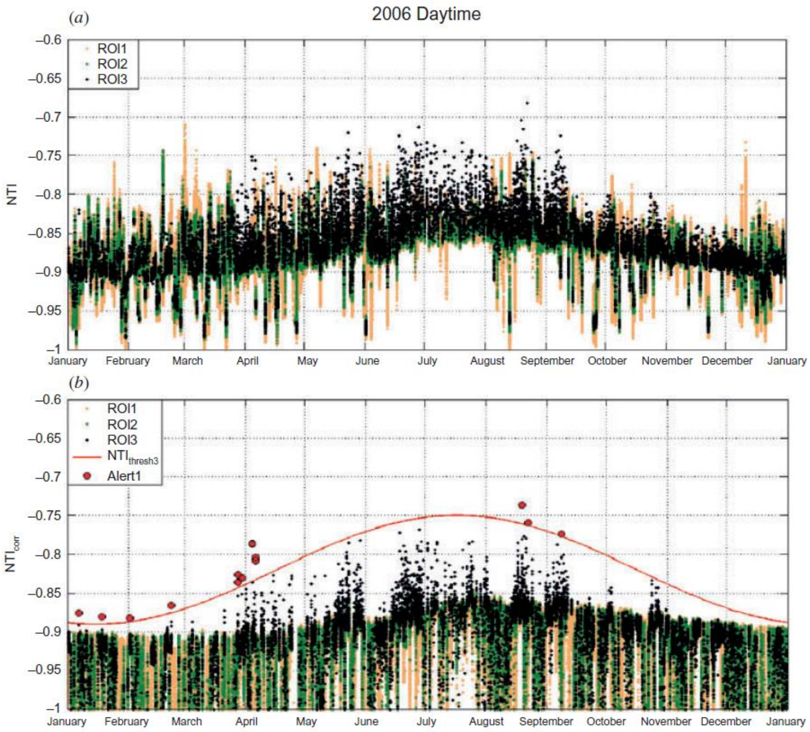
(a)
2006 Daytime
ROI1
ROI2
ROI3
NTI
January February March April May June July August September October November December January
(b)
ROI1
ROI2
ROI3
NTI thresh3
Alert1
NTIcorr
January February March April May June July August September October November December January

Fig. 5

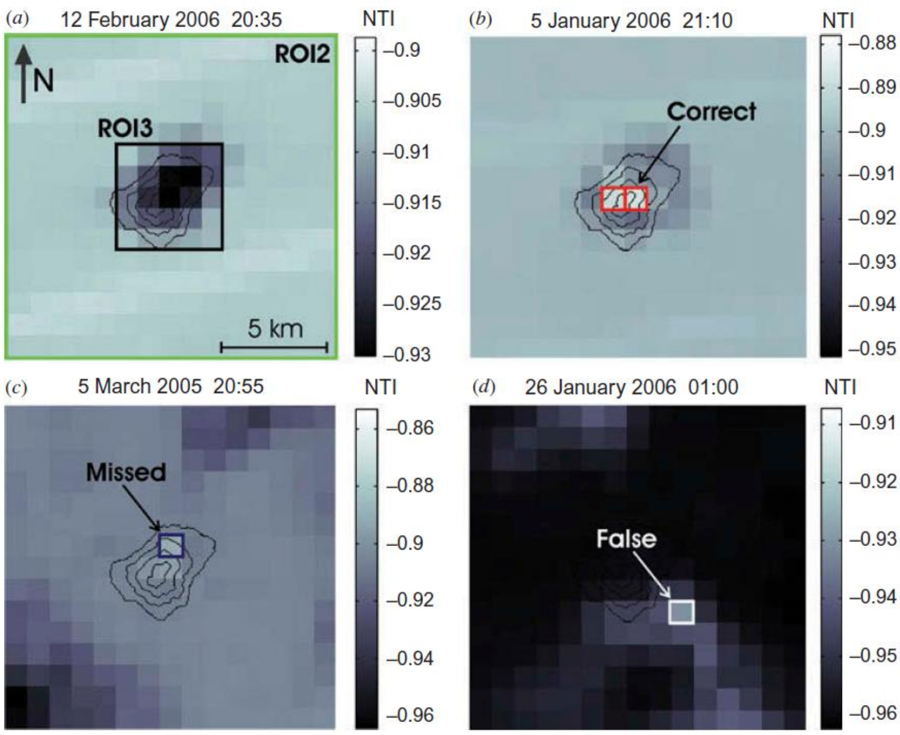
(a) 12 February 2006 20:35
NTI
ROI2
N
ROI3
5 km
(b) 5 January 2006 21:10
NTI
Correct
(c) 5 March 2005 20:55
NTI
Missed
(d) 26 January 2006 01:00
NTI
False

Fig. 6

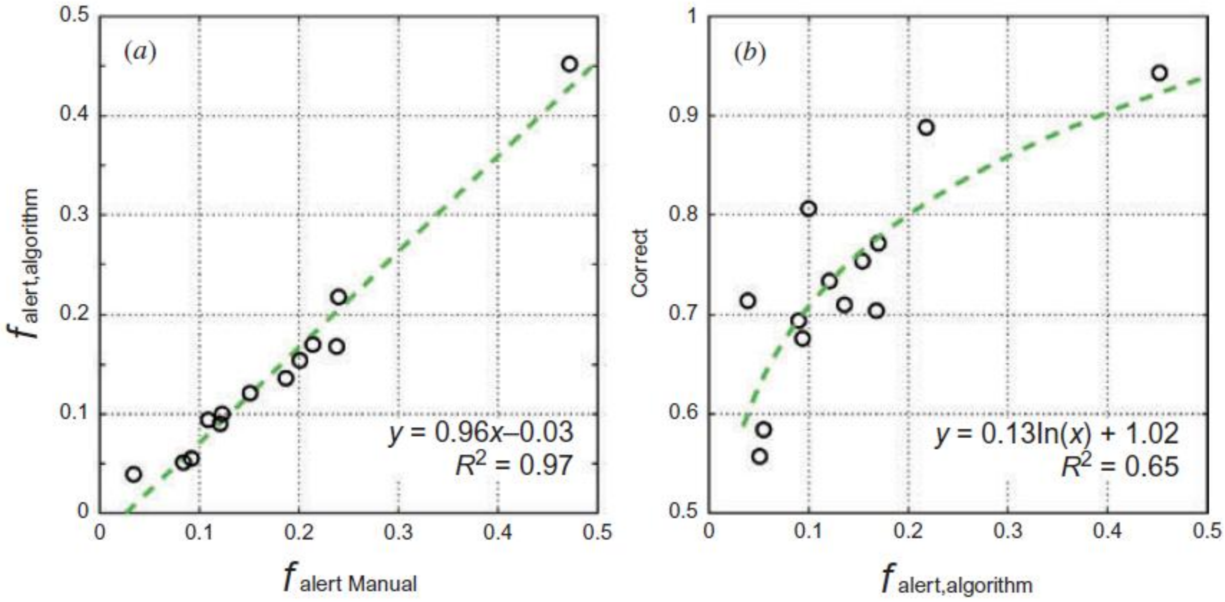
(a)
y = 0.96x–0.03
R^2 = 0.97
$f_{alert,algorithm}$
$f_{alert Manual}$
(b)
y = 0.13ln(x) + 1.02
R^2 = 0.65
Correct
$f_{alert,algorithm}$

Fig. 7

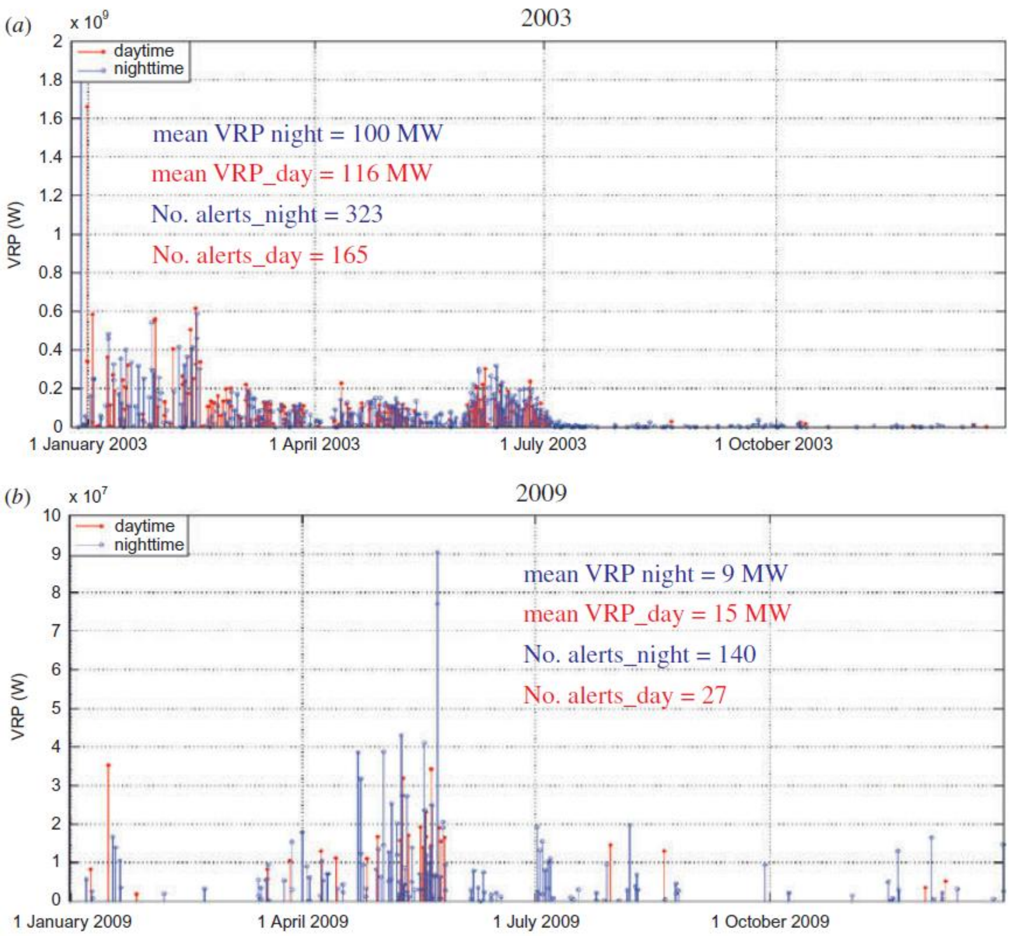
(a)
x 10^9
2003
daytime
nighttime
mean VRP night = 100 MW
mean VRP_day = 116 MW
No. alerts_night = 323
No. alerts_day = 165
VRP (W)
1 January 2003
1 April 2003
1 July 2003
1 October 2003
(b)
x 10^7
2009
daytime
nighttime
mean VRP night = 9 MW
mean VRP_day = 15 MW
No. alerts_night = 140
No. alerts_day = 27
VRP (W)
1 January 2009
1 April 2009
1 July 2009
1 October 2009

Fig. 8

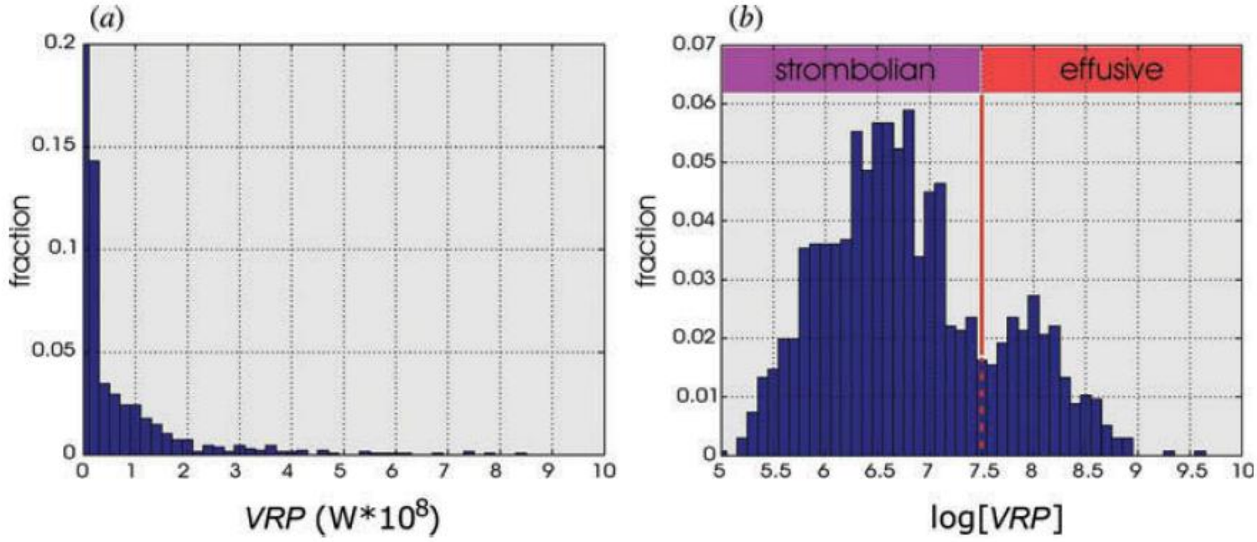
(a)
fraction
VRP (W*10^8)
(b)
strombolian
effusive
fraction
log[VRP]

Fig. 9

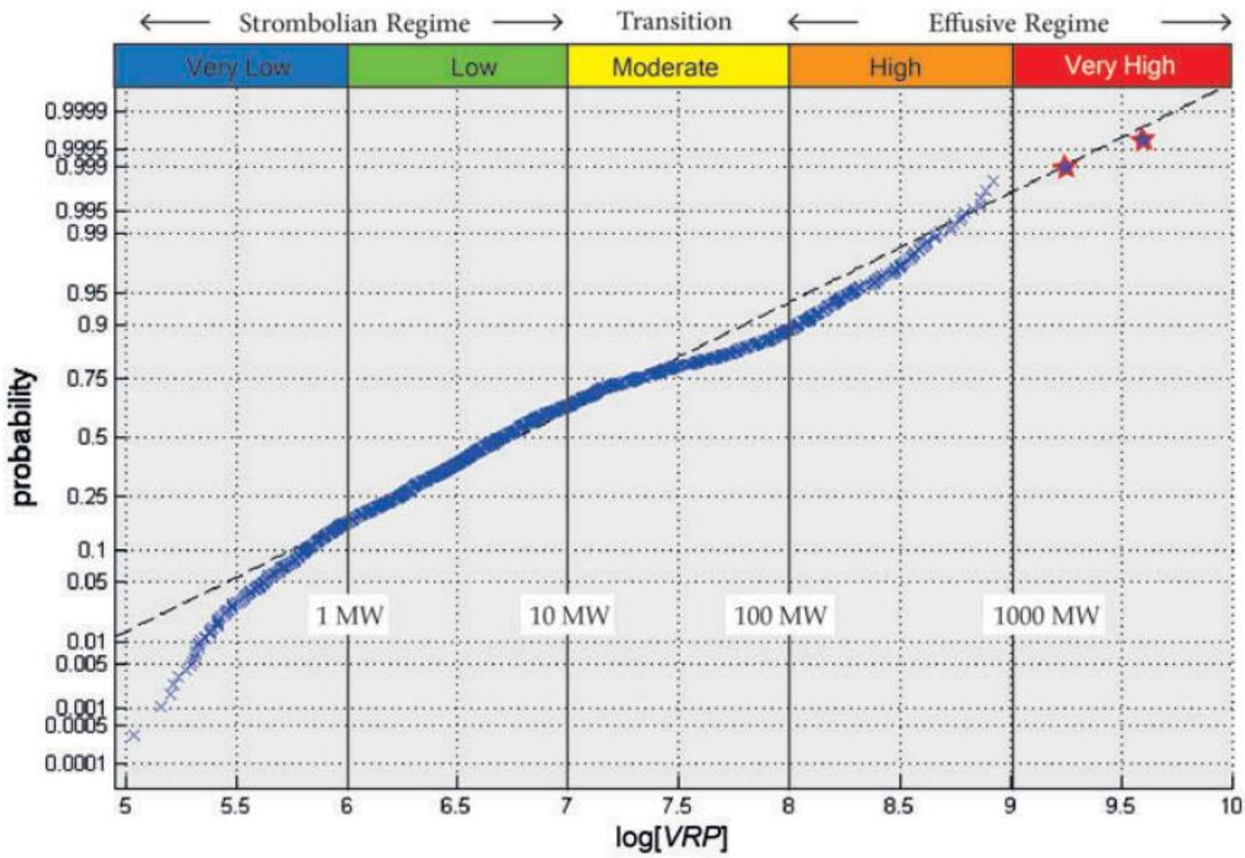
Strombolian Regime
Transition
Effusive Regime
Very Low
Low
Moderate
High
Very High
probability
1 MW
10 MW
100 MW
1000 MW
log[VRP]

Fig. 10

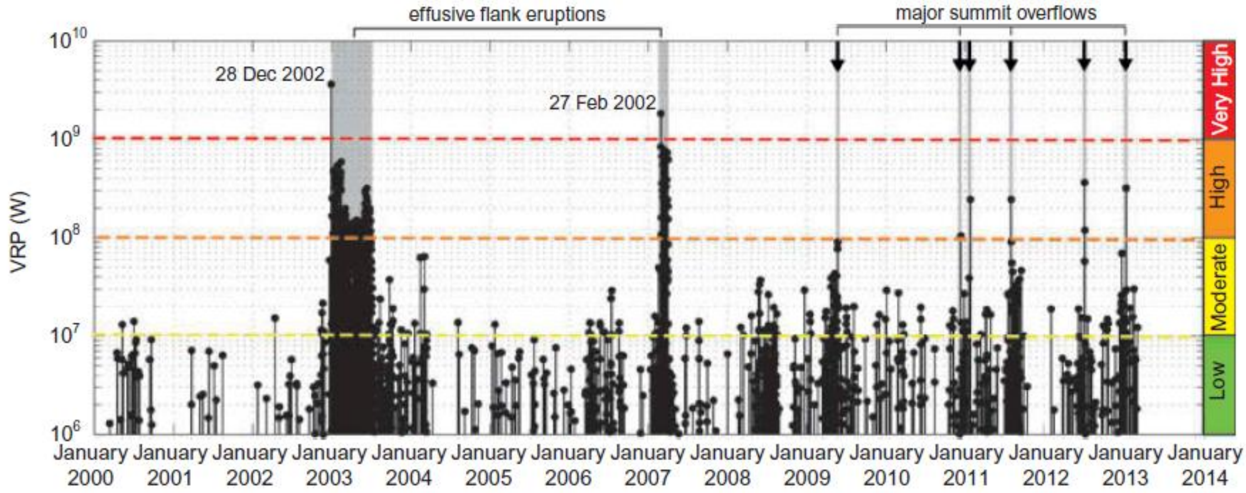
effusive flank eruptions
major summit overflows
28 Dec 2002
27 Feb 2002
VRP (W)
10^{10}
10^9
10^8
10^7
10^6
Very High
High
Moderate
Low
January 2000
January 2001
January 2002
January 2003
January 2004
January 2005
January 2006
January 2007
January 2008
January 2009
January 2010
January 2011
January 2012
January 2013
January 2014

Fig. 11

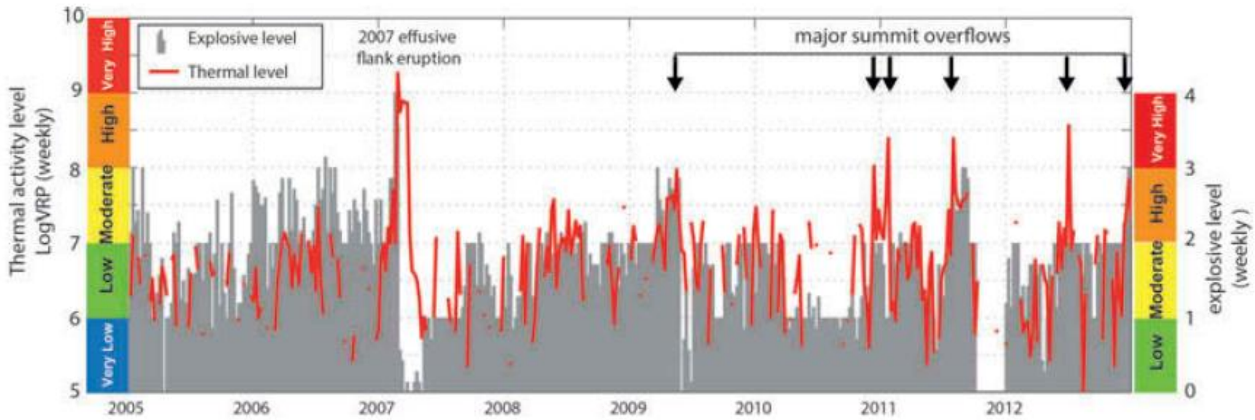
Explosive level
Thermal level
2007 effusive flank eruption
major summit overflows
Thermal activity level LogVRP (weekly)
explosive level (weekly)
Very High
High
Moderate
Low
Very Low
2005
2006
2007
2008
2009
2010
2011
2012

Fig. 12

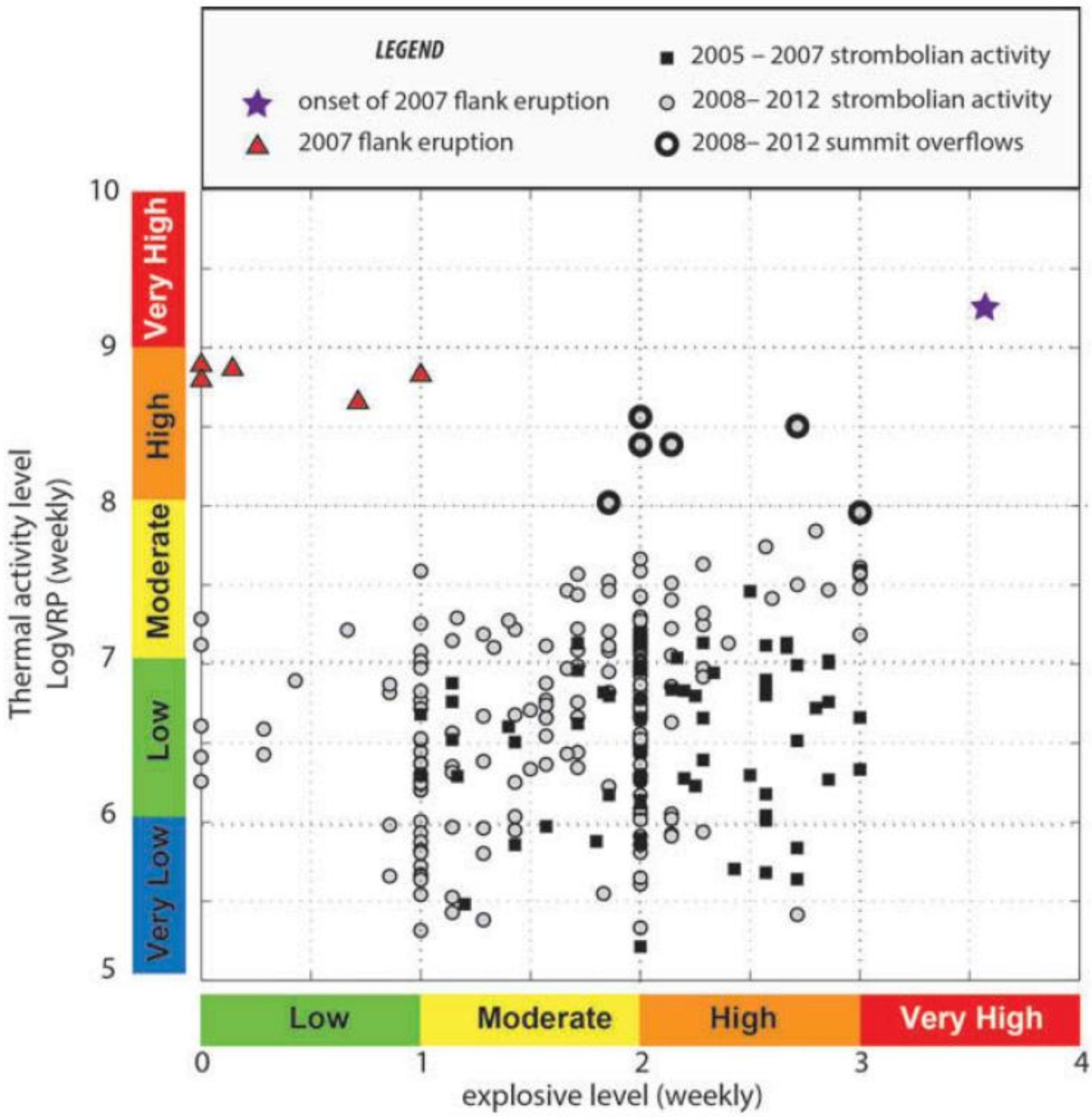

LEGEND
onset of 2007 flank eruption
2007 flank eruption
2005 – 2007 strombolian activity
2008– 2012 strombolian activity
2008– 2012 summit overflows
Thermal activity level
LogVRP (weekly)
Very High
High
Moderate
Low
Very Low
10
9
8
7
6
5
Low
Moderate
High
Very High
0
1
2
3
4
explosive level (weekly)